PHILOSOPHICAL TRANSACTIONS OF THE ROYAL SOCIETY A MATHEMATICAL, PHYSICAL & ENGINEERING SCIENCES

A review of European code-validation studies in high-enthalpy flow

J. Muylaert, L. Walpot and D. Vennemann

Phil. Trans. R. Soc. Lond. A 1999 **357**, 2249-2278
doi: 10.1098/rsta.1999.0430

A review of European code-validation studies in high-enthalpy flow

By J. Muylaert, L. Walpot and D. Vennemann

ESA-ESTEC, Noordwijk, The Netherlands

The paper focuses on the experiments performed in the European high-enthalpy facilities during the manned space flight hypersonic ground testing technology programme. Emphasis is placed on simple configuration testing enabling validation of the physical modelling within non-equilibrium Navier–Stokes codes. The high-enthalpy facilities used are the ONERA hot-shot F4 and the DLR Stalker tube HEG. The simple configurations are the nozzle, the Electre blunt cone, the hyperboloid flare, and the 70° blunt cone. In addition to these axisymmetric configurations, the Halis/Orbiter configuration was extensively tested and numerically computed to validate the ground-to-flight extrapolation methodology. Real-gas effects on aerodynamic forces and in particular on pitching moment for the Halis have been reproduced in the F4 and compared with flight. The paper concludes with a series of recommendations for additional improvements in nozzle calibrations using non-intrusive methods, and for an increased use of computational fluid dynamics for the design of experiments, the definition of the test environment, the interpretation of the results and for extrapolation to flight.

Keywords: high enthalpy; non-equilibrium Navier–Stokes; generic model testing; nozzle flow quality; shock tube; code validation

1. Introduction

As part of the Hermes programme, the European Space Agency (ESA) decided to improve the European wind tunnel infrastructure. This resulted in the construction of the hot-shot F4 at ONERA Le Fauga and the Stalker tube HEG at DLR Göttingen. When the Hermes programme was terminated, a technology programme was initiated covering hypersonic ground testing, capsule aerothermodynamics, and parachute technology, as well as a technology demonstration flight with the atmospheric re-entry demonstrator (ARD), which is an Apollo-like capsule that performed a successful flight in October 1998. The hypersonic ground testing technology programme included development of instrumentation for flow quality assessment and detailed nozzle calibrations for code validation. Thanks to this technology programme, the ESA has improved the tools of design for its future programmes, such as a crew return vehicle, crew transport vehicle and future launchers.

2. Methodology for use of high-enthalpy facilities for design

Figure 1 shows the approach used to validate a methodology for extrapolation of test data to flight conditions. The right branch shows the classical testing in cold wind

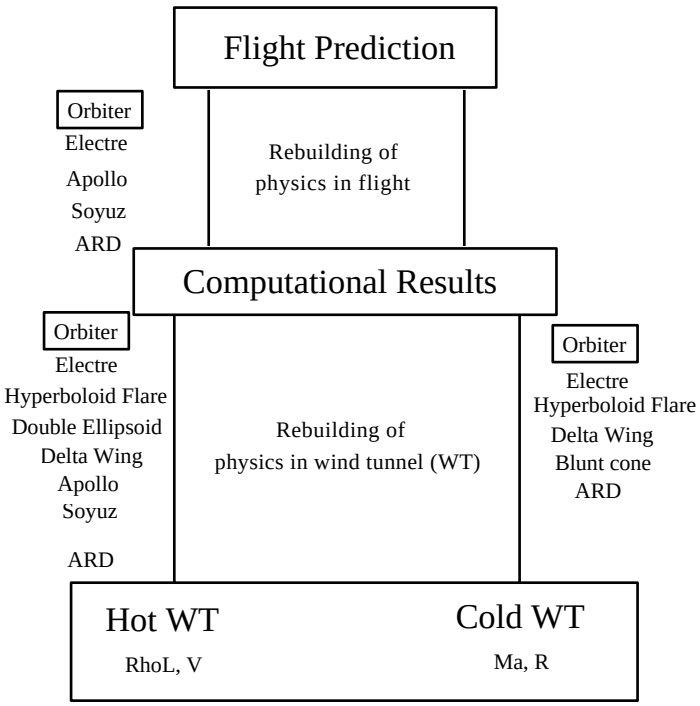

Figure 1. Methodology for extrapolation to flight.

tunnels where Mach and Reynolds number simulation is possible and where code validation for perfect-gas phenomena is feasible. Some examples of generic models tested are the hyperboloid flare for the study of boundary-layer separation and reattachment, and associated turbulent shock boundary-layer interaction; the 70° blunt cone for the study of the wake and its shear layer transition; and the Electre blunt cone for detailed study of nozzle flow quality. On the left branch of the figure are similar generic models for the study of real-gas effects; the facilities used for real-gas testing are the F4 hot shot at ONERA and the HEG Stalker tube at DLR.

In order to study the uncertainties associated with extrapolation to flight it is necessary to test flown configurations in the so-called cold hypersonic facilities as well as in the high-enthalpy facilities. Computations at wind tunnel as well as at flight conditions must be performed. The Orbiter/Halis was selected as the configuration for the study of extrapolation to flight conditions. It is through a computational reconstruction of wind-tunnel conditions, including nozzle expansion processes, that a study of the uncertainties associated with extrapolation to flight can be performed. This computational reconstruction will provide a better understanding of the performance of these facilities and their associated measurement techniques. Obviously, this implies the availability of validated three-dimensional non-equilibrium Navier–Stokes codes or Euler codes coupled with boundary-layer codes.

This validation process goes hand in hand with the process of improving understanding in facility performance and measurement techniques.

A summary review will be given of a recent high-enthalpy validation workshop (Durand *et al.* 1997). The workshop test-case definitions are as given by Schwane (1996).

Table 1. *Features of computational tools*

	CIRA	DLR	ESTEC	ONERA
NS eq.	full NS[a]	thin-layer	thin-layer	PNS[b]
num.	F.D.S	Roe	Roe	van Leer
scheme	F.V.S			Osher
chem.	Park 89	Park 85	Dunn & Kang	Gardiner
vibr.	vibr.	Landau–Teller	Landau–Teller	Landau–Teller
model	equil.	Mill. & White	Mill. & White	Mill. & White
coupl.	—	V-D Park	V-D Park	V-D Park
visc.	Blottner	Blottner	Blottner	Blottner
cond.	Eucken–Wilke	Eucken–Wilke	Eucken–Wilke	Eucken–Wilke
Lewis	1.4	1.4	1.2	1.2

[a]Navier–Stokes.
[b]Parabolized Navier–Stokes.

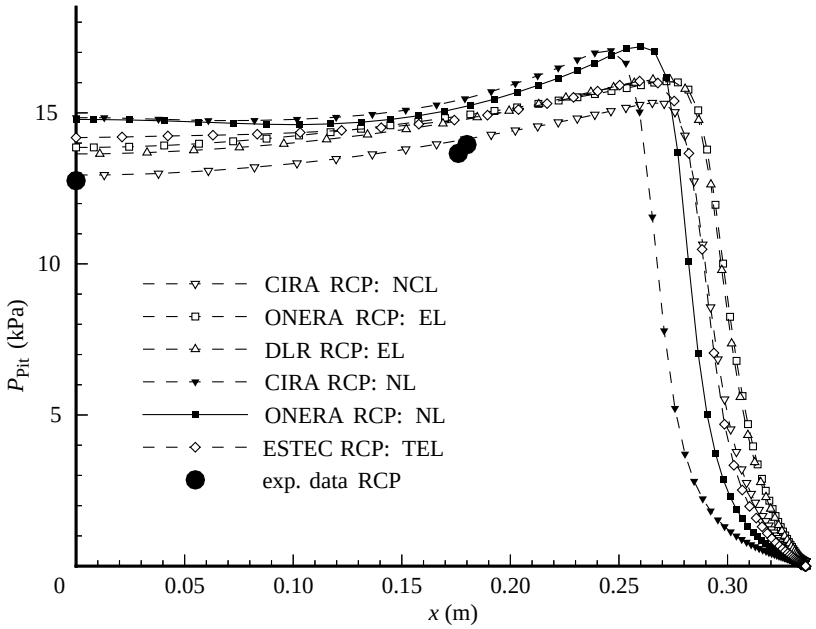

Figure 2. F4 nozzle Pitot distribution (Pitot pressure in section $x = 3.42$ m; NCL, non-equilibrium coupled laminar; TEL, thermochemical equilibrium laminar; EL, equilibrium laminar; NL, non-equilibrium laminar).

3. F4 nozzle

The reservoir conditions for the F4 nozzle are $P_0 = 300$ bar and $H_0/RT_0 = 165$ reduced enthalpy with $R = 288.59\ \mathrm{J\ kg^{-1}\ K^{-1}}$ and $T_0 = 273.5$ K. The computations were performed assuming equilibrium and vibrationally-chemically non-equilibrium flow using laminar, isothermal, fully catalytic wall ($T_w = 300$ K) conditions.

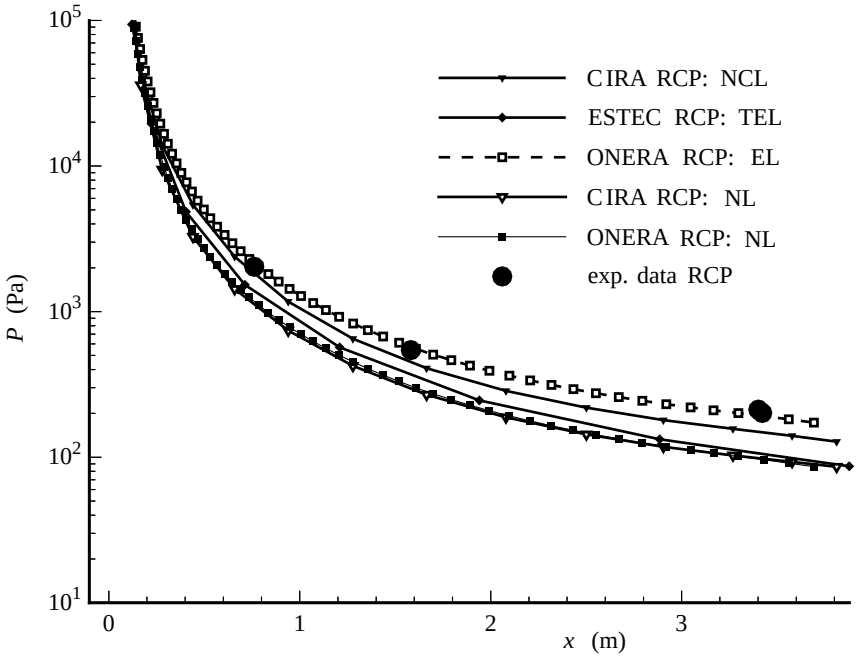

Figure 3. F4 nozzle wall static pressure (reference control point (RCP) $H_0/RT_0 = 165$, $P_0 = 300$ bar (wall pressure); NCL, non-equilibrium coupled laminar; TEL, thermochemical equilibrium laminar; EL, equilibrium laminar; NL, non-equilibrium laminar).

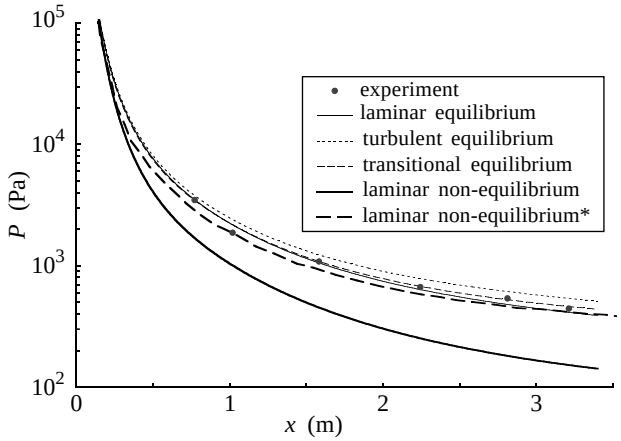

Figure 4. Experimental F4 nozzle static pressure compared with two-dimensional computations with different thermochemical and boundary-layer assumptions ($P_i = 430$ bar, $H_0/RT_0 = 260$ (computations with PNS code PANASCE and CIRA NS code)). *Laminar non-equilibrium with Park's coupling, $q = 0.5$ (CIRA NS).

Computations were performed by the ONERA, DLR, CIRA and ESTEC. The characteristics of these computations are shown in table 1.

Figure 2 shows the comparison between the measured Pitot distribution at the nozzle exit. The Pitot data agree best with the CIRA computations where Park's

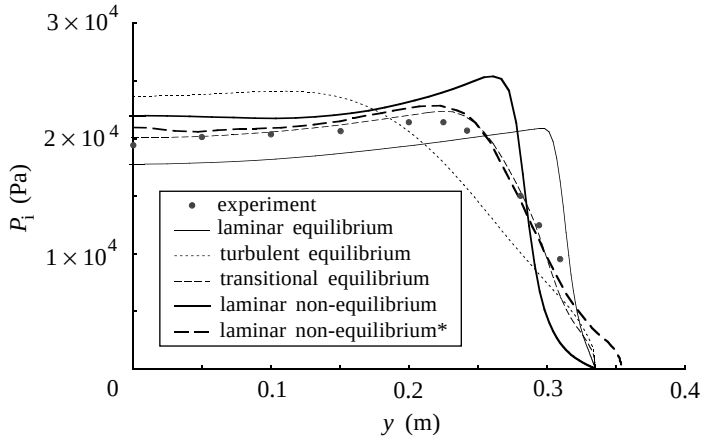

Figure 5. Experimental F4 free-stream stagnation pressure compared with two-dimensional computations with different thermochemical and boundary-layer assumptions (P_i = 430 bar, H_0/RT_0 = 260 (computations with PNS code PANASCE and CIRA NS code)). *Laminar non-equilibrium with Park's coupling, $q = 0.5$ (CIRA NS).

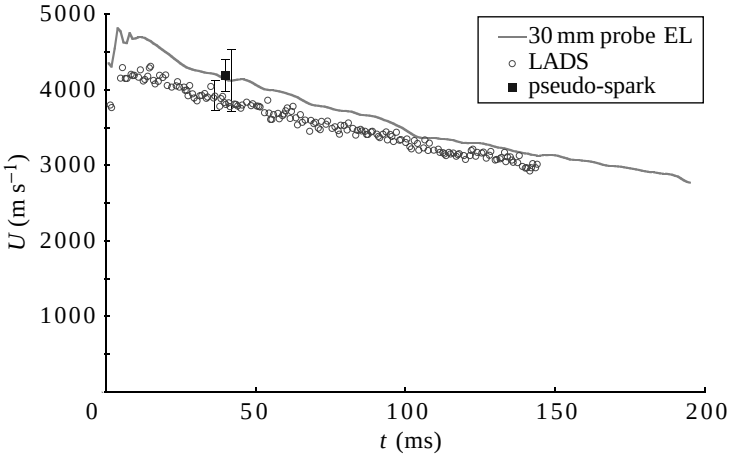

Figure 6. Free-stream velocities from LADS, pseudo-spark electron gun and modellings (from sphere stagnation heat transfer and stagnation pressure assuming equilibrium and laminar nozzle boundary layer (run 834). EL, equilibrium laminar.

vibration dissociation recombination (VDR) coupling was used. This means that reaction-rate constants are computed not only with the translational temperature but with a geometric average of translational and vibrational temperatures $\sqrt{TT_v}$. This coupling speeds up the computation of the chemistry, resulting in macroscopic variables such as pressure or temperature close to equilibrium.

Figure 3 shows the wall static pressure distributions, which agree well with the laminar equilibrium computations. The computed values vary from 80 Pa for the non-equilibrium case to 180 Pa for the equilibrium case. At this stage, these results were not satisfactory as it was not clear why Pitot data are closer to non-equilibrium values and wall static data closer to laminar equilibrium. Different thermochemical assumptions were combined with different wall-boundary assumptions. Figures 4 and

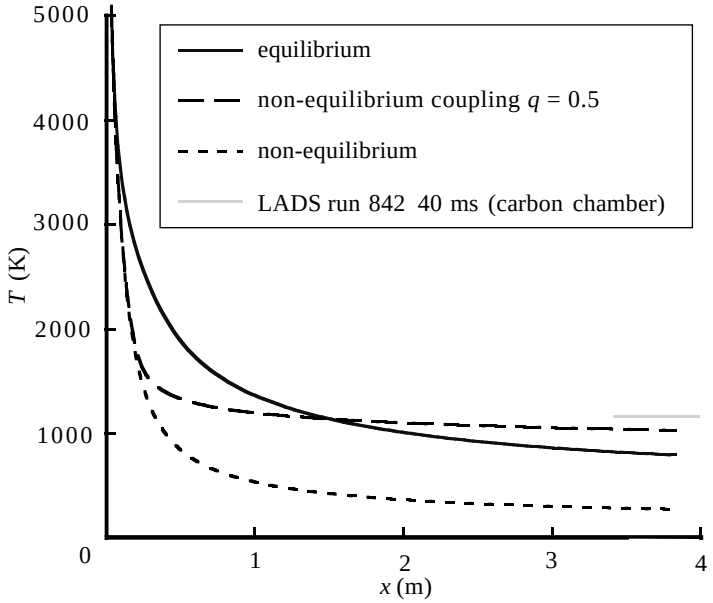

Figure 7. F4 nozzle translational temperature distributions from experiment and one-dimensional Euler computations at equilibrium and non-equilibrium with and without VDR ($P_0 = 404$ bar, $H_0/RT_0 = 170$).

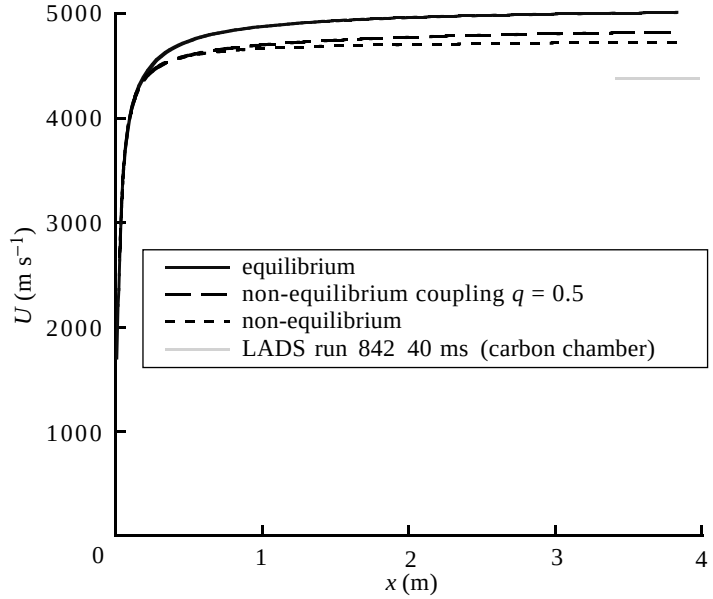

Figure 8. F4 nozzle velocity distributions from experiment and one-dimensional Euler computations at equilibrium and non-equilibrium with and without VDR ($P_0 = 404$ bar, $H_0/RT_0 = 170$).

5 show that good comparisons are obtained for the transitional wall-boundary layer, i.e. when it is assumed that transition starts at the throat and ends at the nozzle exit (combined with equilibrium flow or when a laminar boundary layer is assumed to be

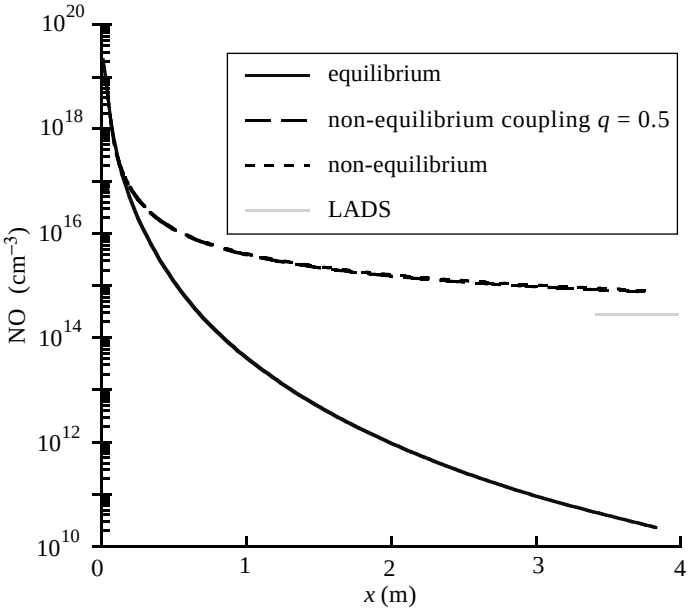

Figure 9. F4 nozzle NO concentration distributions from experiment and one-dimensional Euler computations at equilibrium and non-equilibrium and with and without VDR ($P_0 = 404$ bar, $H_0/RT_0 = 170$).

combined with the non-equilibrium VDR coupling). Recently, the copper chamber was replaced by a carbon chamber in order to reduce contaminants in the flow. Figure 6 shows the free-stream velocities as measured by different redundant means: from laser diode spectroscopy (LADS), the pseudo-spark, electron gun and from sphere stagnation heat transfer and stagnation pressure assuming equilibrium and a laminar nozzle boundary layer (see Sagnier & Verant 1998). Thanks to the lower level of contaminants and improved heat-flux measurements, a reliable means of measuring the reservoir enthalpy has now been validated. Figures 7–9 show the good comparison between measured and computed temperature, velocity and NO concentrations when using the VDR coupling.

It can be concluded that, regardless of the arc option, the nozzle flow is close to equilibrium at high-enthalpy conditions. It is very likely that such nozzle behaviour is caused by the physics of flow expansion and not by quenching of some contaminant. Cross-checking this behaviour with other nozzles would be very welcome so as to verify this assumption.

4. HEG nozzle

The reservoir condition for the HEG nozzle test case is 386 bar and reduced enthalpy $H_0/RT_0 = 268$.

Figure 10 compares the iso-Mach number lines for equilibrium and non-equilibrium computed flow. For the non-equilibrium case the flow pattern is changed due to recompression waves emerging from the nozzle wall. This effect is clearly visible on the nozzle centreline static pressure distribution as seen in figure 11. The static pressure is most sensitive to thermochemical effects. At the nozzle exit the static

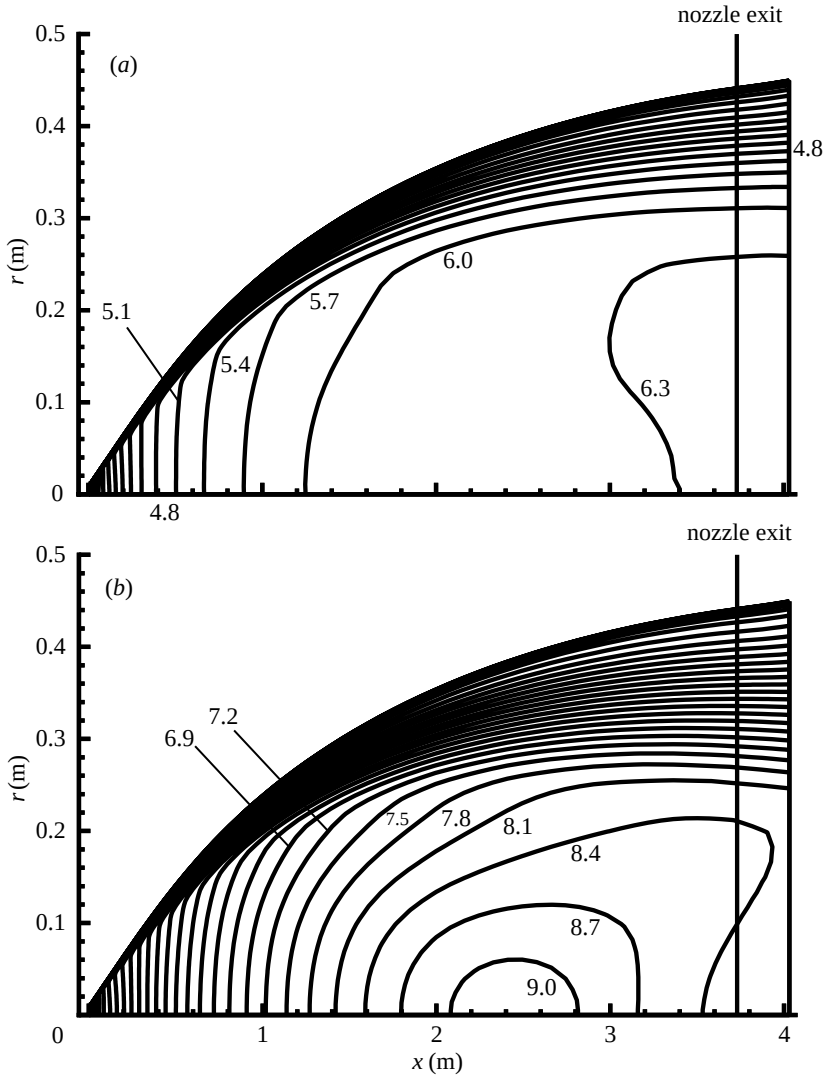

Figure 10. Iso-Mach number lines for (*a*) equilibrium and (*b*) non-equilibrium flow.

pressure for equilibrium flow is nearly twice the equivalent non-equilibrium value. This confirms the importance of having high-quality static centreline pressures to characterize the thermochemical state of the free stream.

As with the static pressure along the nozzle axis, the wall pressures in the non-equilibrium case are lower than in the equilibrium case. The comparison between numerical and experimental wall pressures clearly suggests that the flow is non-equilibrium.

It is surprising to see in figure 11 that the delayed transition in the DLR computations influences the centreline pressures but not the wall pressures. This may indicate that due to the delayed transition the boundary layer does not change too much, but that the flow is mainly induced by waves generated in the transition region. This is confirmed by the wavy pattern of the Pitot pressures as seen in figure 12. This figure

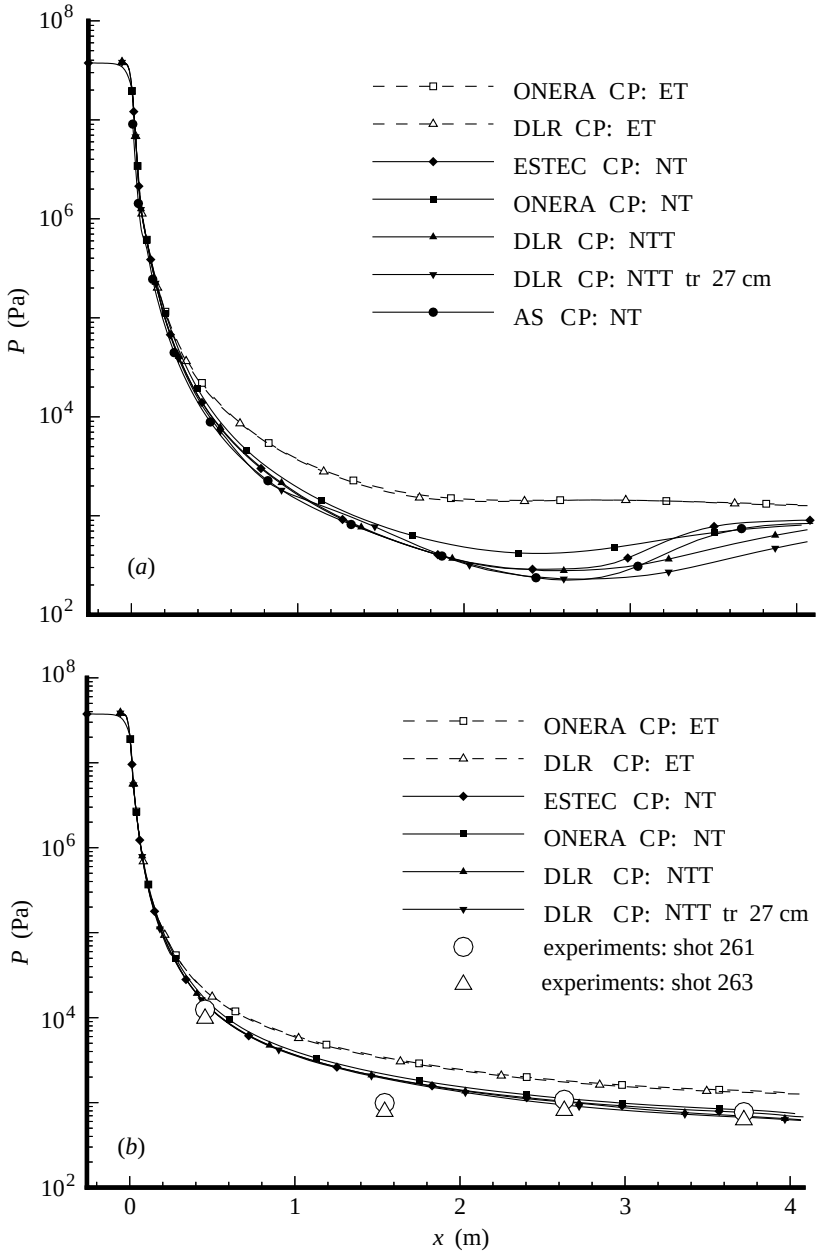

Figure 11. Pressure along the HEG nozzle wall: (*a*) pressure along the nozzle axis; (*b*) pressure along the nozzle wall. ET, equilibrium turbulent; NT, non-equilibrium turbulent; NTT, non-equilibrium turbulent throat; tr 27 cm denotes transition as having been switched at a position 27 cm downstream of the throat (see DLR computations).

shows the Pitot profiles at the nozzle exit, and at 111 mm and 305 mm downstream of the nozzle exit.

In figure 12 the boundary-layer thickness as computed with the Edenfield corre-

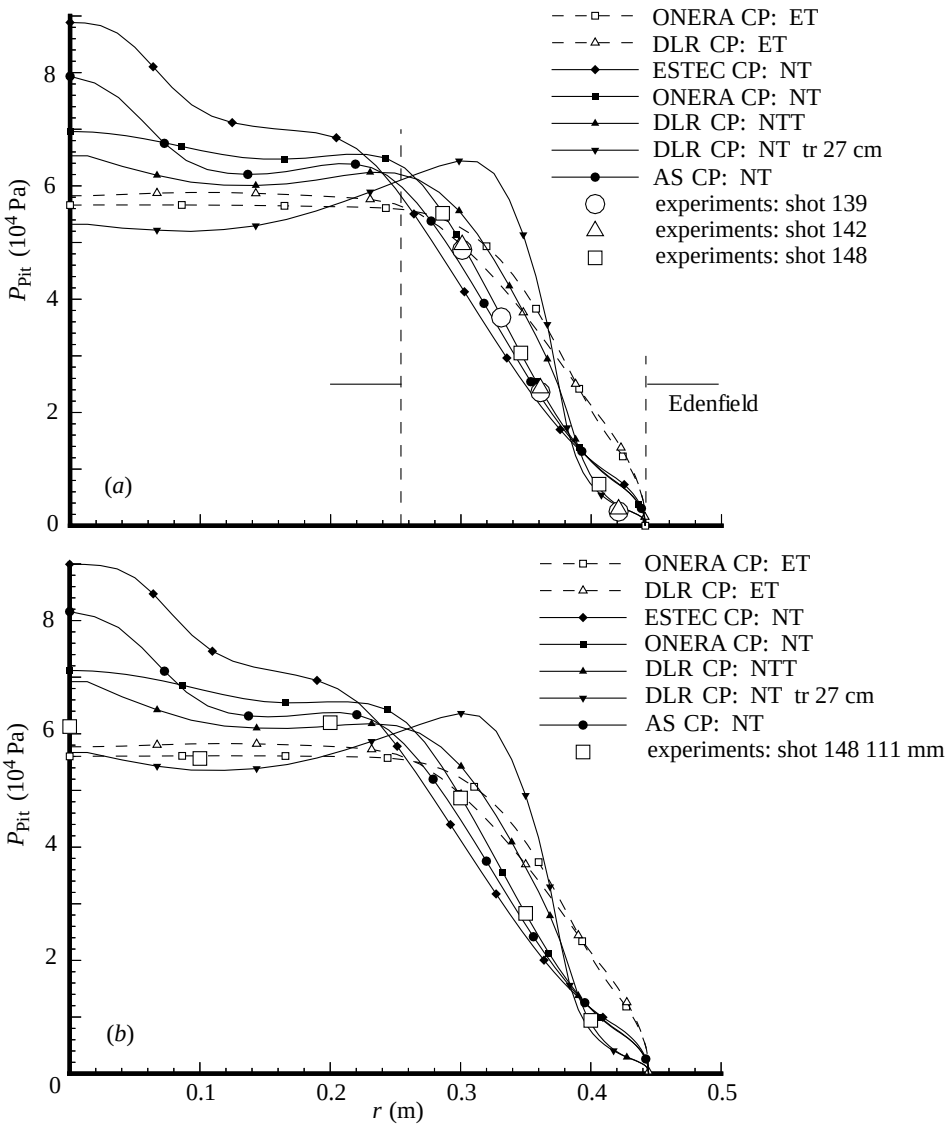

Figure 12. Pitot pressure profiles for HEG contoured nozzle ($P_0 = 386$ bar, $H_0/RT_0 = 268$): (a) Pitot pressure along the nozzle exit; (b) Pitot pressure in section 111 mm out of exit.

lation compares well with the measured and computed turbulent non-equilibrium data. This confirms that along the main part of the nozzle wall the boundary layer is turbulent. For all three Pitot pressure locations the numerical results show significant scatter on the axis of the order of 22%. This directly corresponds to the uncertainty in the free-stream density. It is interesting to note that in the core flow the experiments seem to fit better with the equilibrium values than with the non-equilibrium values. This contrasts with the wall static pressures, which show a better fit with the non-equilibrium data.

The DLR computation performed with the delayed transition is the only one for

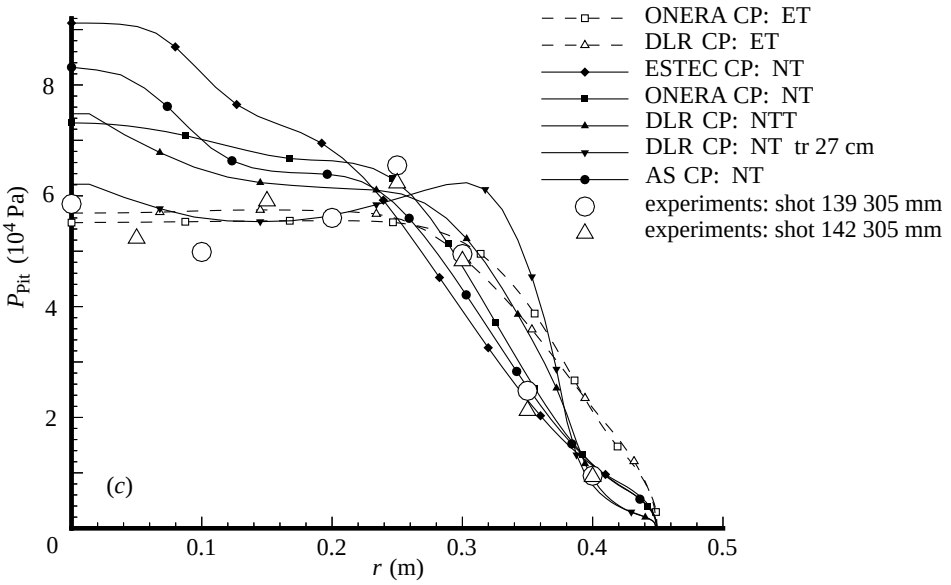

Figure 12. (*Cont.*) (*c*) Pitot pressure in section 305 mm out of exit.

Table 2. *Free-stream conditions for the Electre*

	HEG	F4
T_∞ (K)	790	795
T_{v,N_2} (K)	790	795
T_{v,O_2} (K)	790	795
ρ_∞ (kg m^{-3})	1.640×10^{-4}	5.45×10^{-4}
u_∞ (m s^{-1})	5919	4930
T_w (K)	300	300
C_{N_2}	0.773 254	0.7729
C_N	0.001 877	0.00
C_{O_2}	0.003 901	0.2376
C_O	0.215 092	0.00
C_{NO}	0.005 876	0.00

non-equilibrium that in the core flow region comes close to the experimental data. However, in the boundary layer it does not fit with the experiments. The two computations, with and without delayed transition, demonstrate that the amplitude of the Pitot pressure in the core region can be changed quite arbitrarily by moving the transition location upstream and downstream. In future one should try to measure directly the wall transition position and extent. In conclusion, notwithstanding the fact that very good results have already been achieved both for F4 and the HEG, additional intrusive classical free-stream (as well as non-intrusive) measurements are required to characterize better the level of chemically-vibrationally non-equilibrium flow and to confirm the state of the wall boundary layer, especially the position and extent of transition.

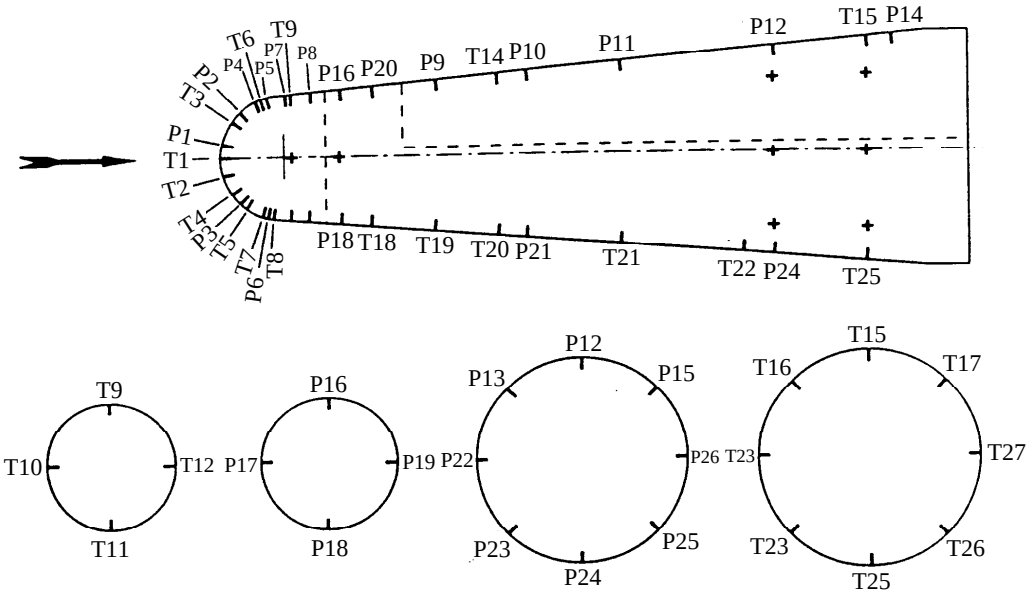

Figure 13. Schematic view of the Electre model.

5. Electre

The geometry of the Electre configuration is available from Durand *et al.* (1997) and from figure 13. The free-stream conditions for F4 and the HEG are given in table 2.

Figures 14–17 show the measured C_p and heat-flux distributions and compare them with the non-equilibrium computations from the different contributions. Full catalytic, as well as non-catalytic, isothermal wall conditions are taken ($T_w = 300$ K). For the pressures, both for F4 as well as for the HEG, good agreement between experiment and computation is obtained at the nose region. For the Electre in F4, the scatter in pressure on the rear part of the cone is within 10%. On the rear part of the cone for the HEG experiments the scatter is larger and can be explained according to Sagnier & Verant (1998) by the range of the pressure transducers (operating range 0–3.5 bar) mounted to suit the F4 experiments and the associated error of *ca.* 3% full scale. Computations in Walpot & Bakker (1997) show that the experimental pressures on the rear part of the cone lie between the equilibrium and non-equilibrium free-stream conditions. Analysing the heating levels in F4 and the HEG is more difficult.

Figure 15 shows that the stagnation-point heat flux is *ca.* 25% higher than computed fully catalytic values. One has to note here that these particular Electre experiments in F4 were carried out with the old copper chamber. Figures 18 and 19 show a comparison of two nearly identical runs where the data during the complete run are shown. During the run, total pressure and enthalpy keep decreasing due to arc-chamber heat and mass loss; however, this process is slow enough to yield quasi-steady-state conditions since the total pressure and enthalpy variation is less than 1%.

Figure 18 corresponds to run 622 with the copper chamber, whereas figure 19 corresponds to run 834 with the new carbon chamber. The description 322b130 on

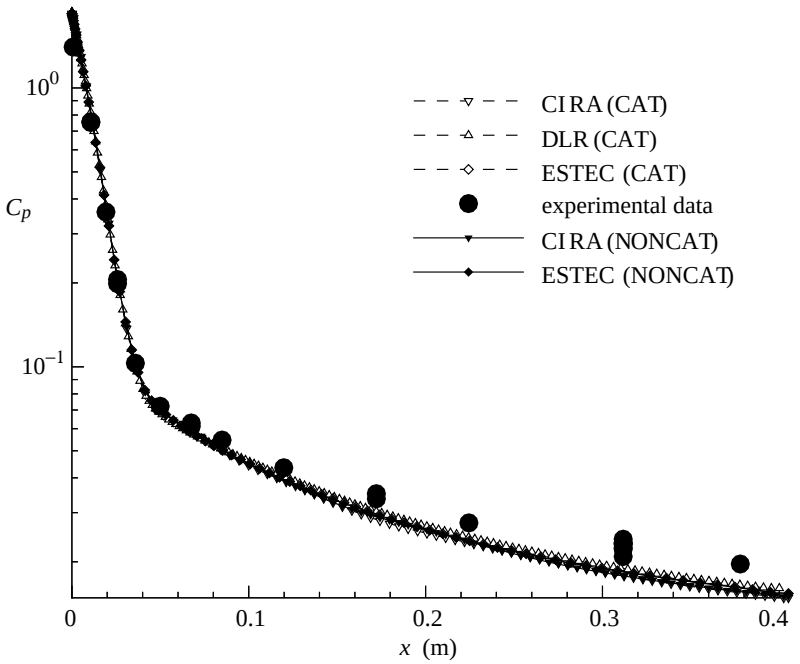

Figure 14. F4 Electre C_p distribution ($P_0 = 300$ bar, $H_0/RT_0 = 165$ (experimental data: $P_0 = 300$ bar, $H_0/RT_0 = 163$)).

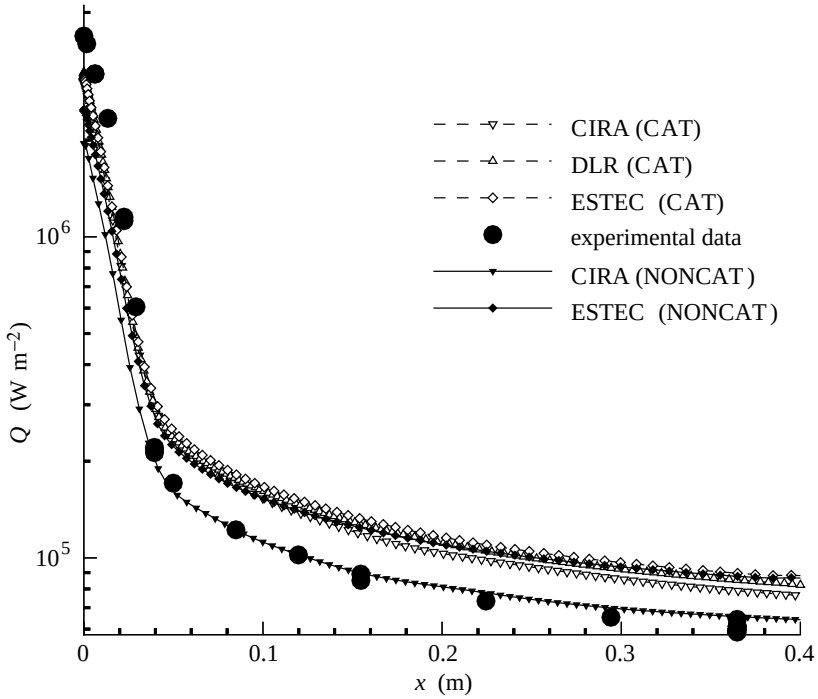

Figure 15. F4 Electre heat flux ($P_0 = 300$ bar, $H_0/RT_0 = 165$ (experimental data: $P_0 = 300$ bar, $H_0/RT_0 = 163$)).

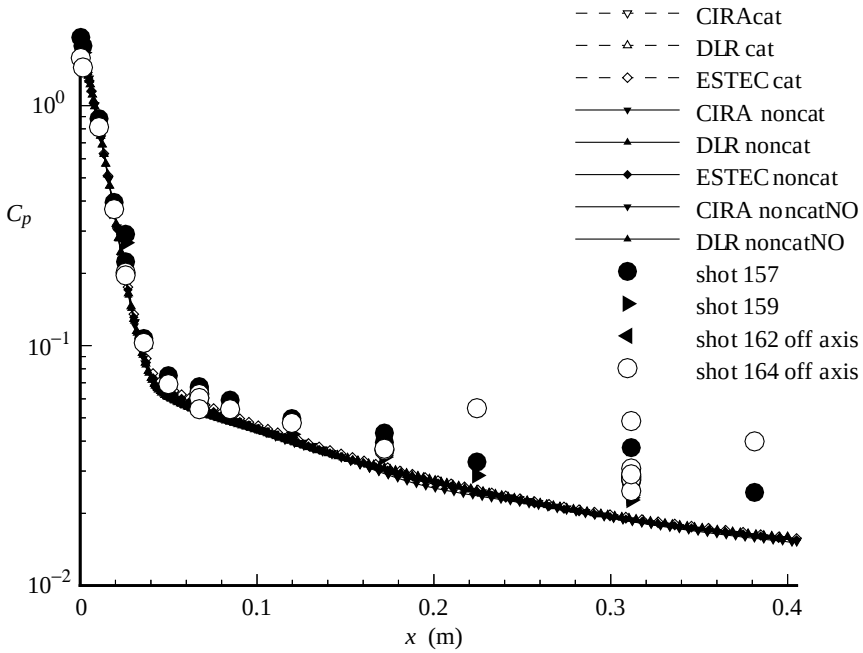

Figure 16. HEG Electre C_p distribution ($P_0 = 386$ bar, $H_0/RT_0 = 268$).

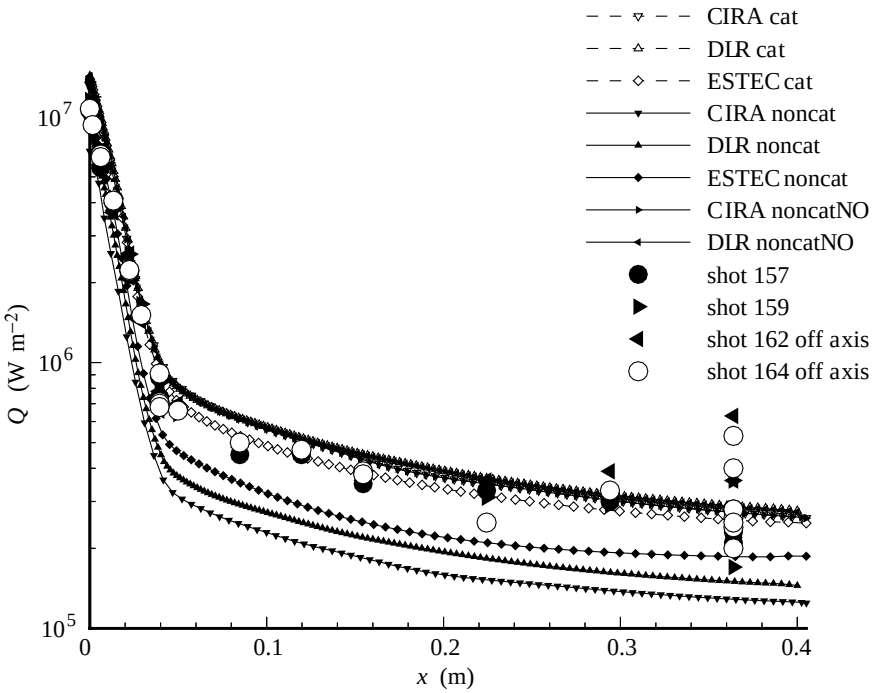

Figure 17. HEG Electre heat-flux distribution ($P_0 = 386$ bar, $H_0/RT_0 = 268$).

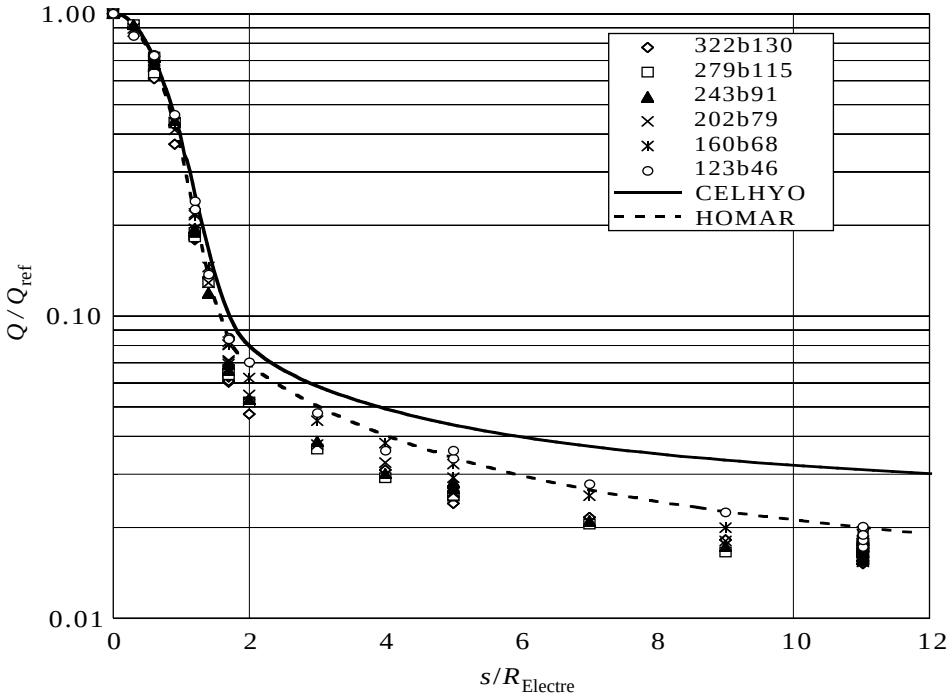

Figure 18. Electre heat flux distribution (copper chamber) run 622 (CELHYO, $M_\infty = 7.2$; HOMAR, $M_\infty = 13$).

figure 18 means reservoir pressure is 322 bar and reduced enthalpy is 130. The better agreement on the rear part of the cone of Electre is due to the reduction in nose heating. As explained in Sagnier & Verant (1998) the reduction of the nose heat flux is due to a reduction of contaminants in the flow for the carbon chamber. The possibility of a catalysis effect due to ageing on the rear part was apparently excluded since new clean gauges were installed, and the experiments revealed no change in heat level (Sagnier & Verant 1998). For figures 18 and 19 the Homar $M = 13$ data are perfect-gas computational results for $M = 13$ free stream. The CELHYO results are non-equilibrium Navier–Stokes computations on Electre with free-stream conditions at $M = 7.2$, corresponding to equilibrium nozzle free stream and at $M = 8.9$ corresponding to non-equilibrium/frozen nozzle flow. This is consistent with earlier findings: as mentioned by Simeonides *et al.* (1996), the influence of equilibrium free stream is seen to yield significantly higher heating rates on the conical afterbody of Electre, as compared with non-equilibrium free-stream results.

Figure 17 shows the heat flux distribution for the Electre tested in the HEG. At the stagnation point the heat flux is best predicted assuming non-catalytic wall conditions. All contributors provide a heat flux of *ca.* 11 MW m^{-2}, which is 20% higher than the experimental value. Since the model is assumed to be close to a catalytic steel model, it could be, according to Walpot & Kordulla (1996), that the actual enthalpy of the flow is lower than the nominal enthalpy computed from the shock speed. An estimate was made by Walpot & Kordulla (1996) that a maximum of 10% of the total enthalpy could be lost by radiation.

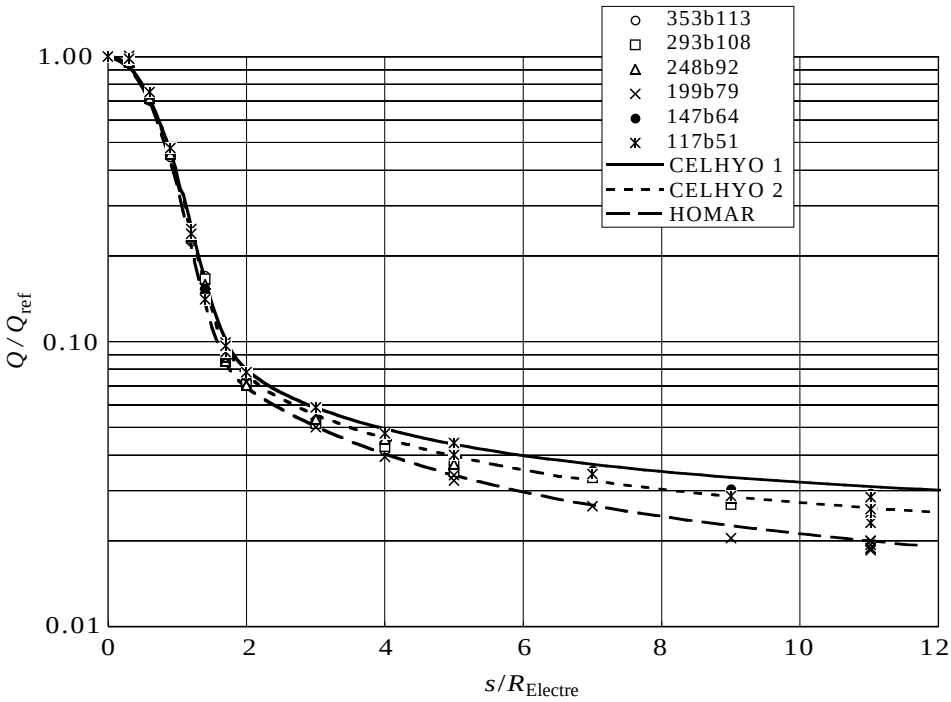

Figure 19. Electre heat flux distribution (carbon chamber) run 834 (CELHYO 1, $M_\infty = 7.2$; CELHYO 2, $M_\infty = 8.9$; HOMAR, $M_\infty = 13$).

Furthermore, it has to be remarked that for this test case the free-stream conditions were chosen to be non-equilibrium; as mentioned above, when approaching equilibrium, a nozzle flow provides higher rear-cone heat fluxes.

6. Hyperboloid flare

The purpose of this test case, defined in Schwane (1996), is to study real-gas and viscous interaction effects on a simple axisymmetric configuration. The configuration is the axisymmetric equivalent for Hermes at 30° angle of attack and with 20° of body-flap deflection. The F4 free-stream conditions are the same as for the Electre test case. Figure 20 shows the Mach number contours. Figures 21 and 22 show the C_p and heat-flux distributions, respectively.

It is shown that the pressure and heating on the forward part match well, whereas no good data are obtained on the flare as the separation length has not been simulated.

The experimentally obtained separation length is smaller than the computationally obtained value, suggesting that the free-stream viscous interaction parameter $M/\sqrt{Re_\infty}$ is higher than proposed in table 2 or, and perhaps most probably, that the shear layer became turbulent. Figure 23 shows the pressure distributions on the hyperboloid flare taken at different instants during run 842 with the improved carbon chamber. A comparison is shown with computations assuming different free-stream conditions. The improvement is due to a reduction in contaminants for the carbon

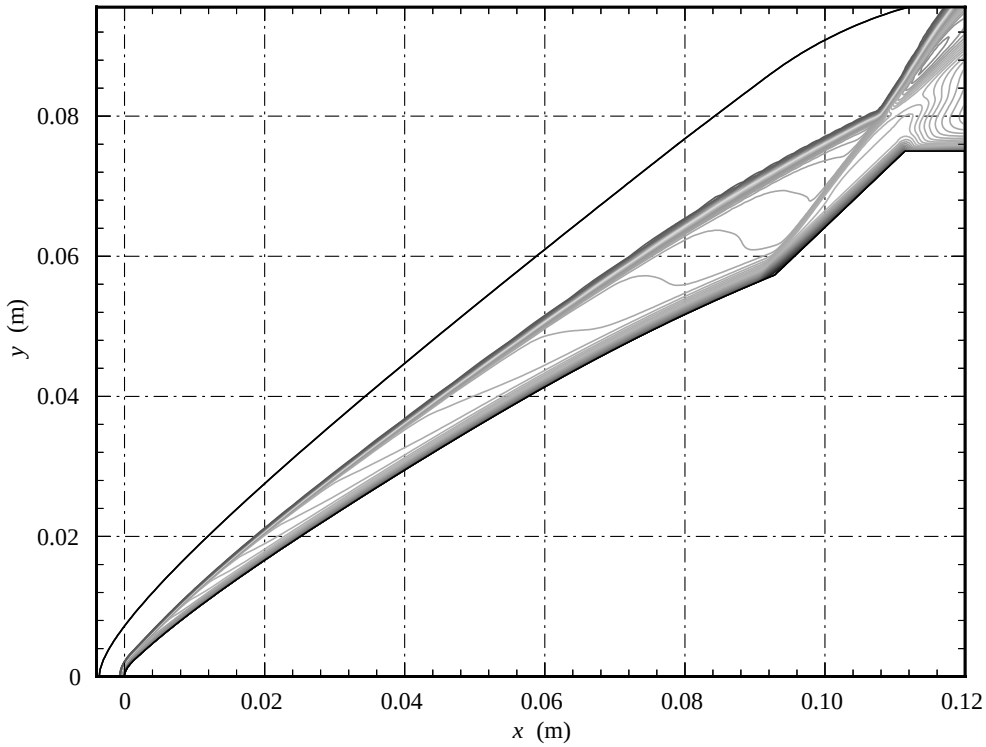

Figure 20. F4 hyperboloid-flare Mach number contours.

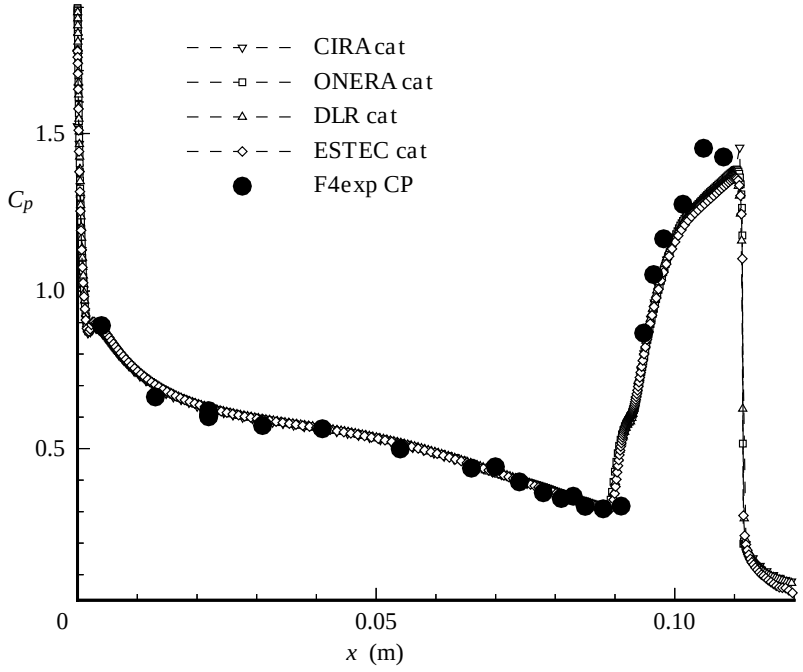

Figure 21. F4 hyperboloid-flare C_p distribution ($P_0 = 300$ bar, $H_0/RT_0 = 165$).

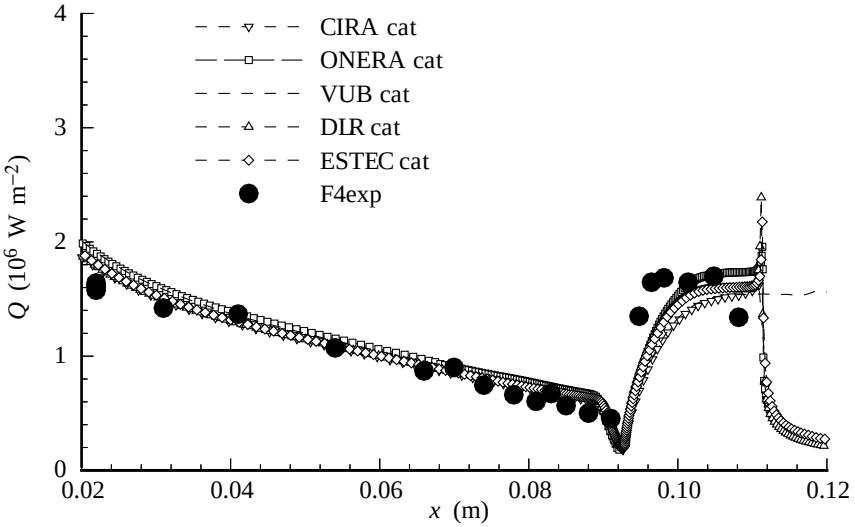

Figure 22. F4 hyperboloid-flare heating ($P_0 = 300$ bar, $H_0/RT_0 = 165$).

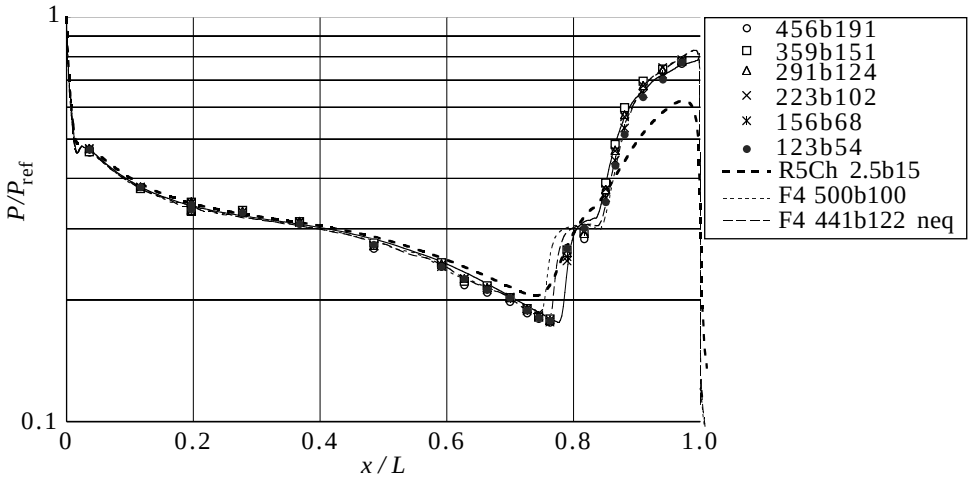

Figure 23. F4 hyperboloid-flare run 842 (carbon chamber).

chamber as compared with those from the copper chamber; this is similar to the conclusion obtained in § 5 for the Electre model.

It is recommended that a better test case should be designed for the study of real-gas effects on boundary-layer separation and reattachment. A larger nose combined with a smaller hyperboloid angle followed by a large flare to fully capture the interaction could be designed. An example of such a design was produced by Holden *et al.* (1997) and should be followed up.

7. 70° blunt cone

Within the AGARD (Advisory Group for Aerospace Research and Development) Fluid Dynamics Panel WG18, the blunt cone has been studied extensively for code-

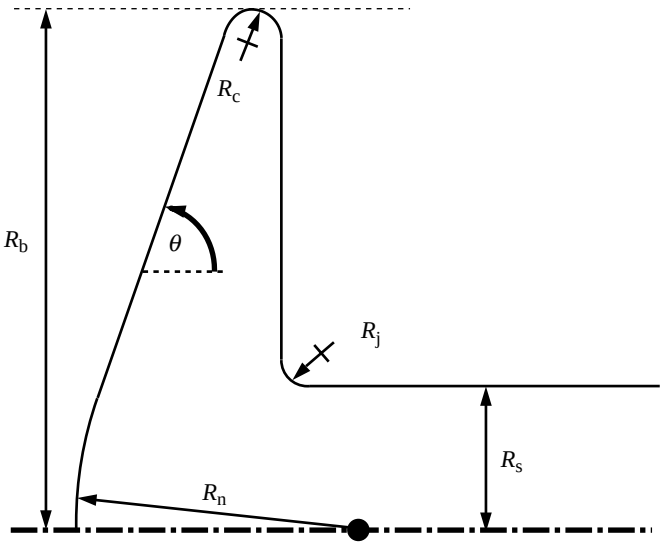

Figure 24. Blunt-cone model geometry. $\theta = 70°$, $R_b = 3.0$ in, $R_n = R_b/2$, $R_c = R_b/20$, $R_s = R_b/4$, $R_j = R_b/12$.

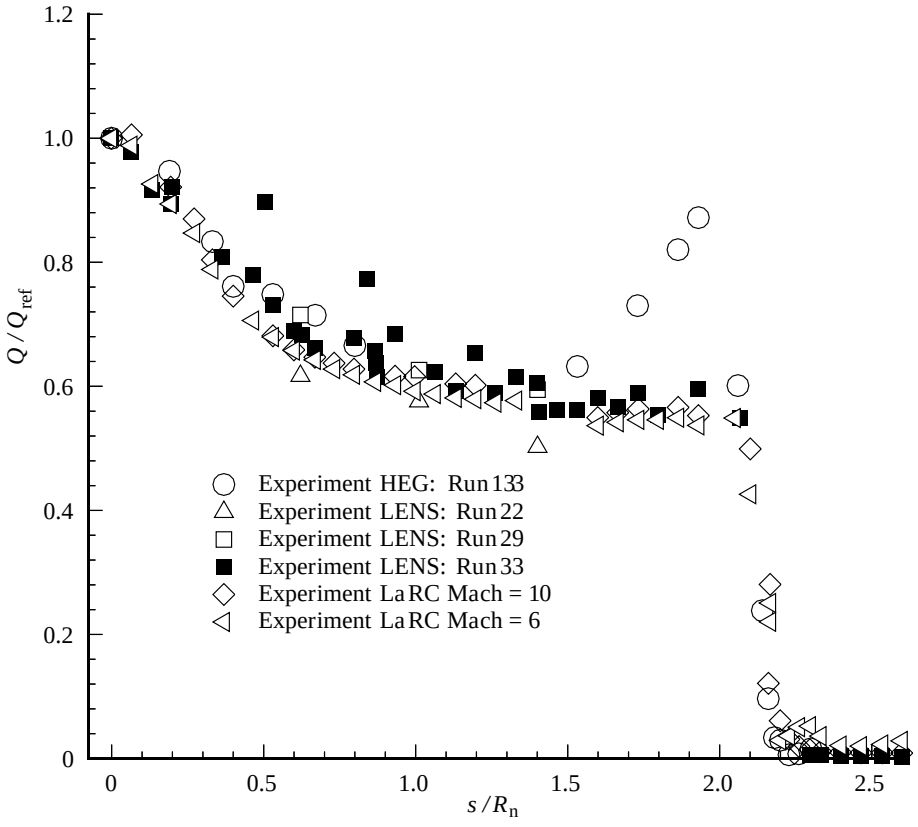

Figure 25. Blunt-cone forebody experimental data in the LENS, HEG and LaRC.

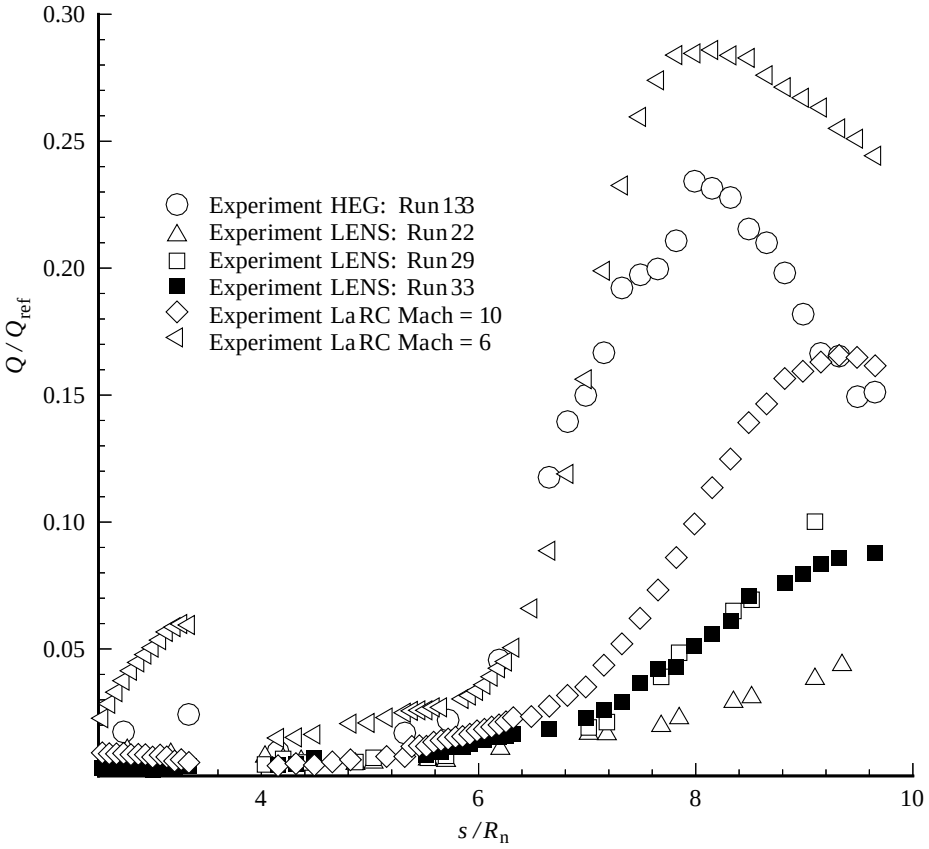

Figure 26. Blunt-cone aftbody experimental data in the LENS, HEG and LaRC.

Table 3. *Operating conditions*

	F4:II	F4:III	F4:IV
P_0 (bar)	320	390	180
H_0 (MJ kg^{-1})	2.1	10.3	12.2
V (m s^{-1})	1899	4401	4669
M	13.8	9.27	8.72
T (K)	46.6	559	711
P (Pa)	74.7	203.5	71.01
ρ (kg m^{-3})	0.005 56	0.001 26	0.000 35
c_{N_2}	0.767	0.767	0.767
c_{O_2}	0.233	0.233	0.233
c_{NO}	—	—	—
c_N	—	—	—
c_O	—	—	—
Re/m	3.6×10^6	1.9×10^5	4.8×10^4

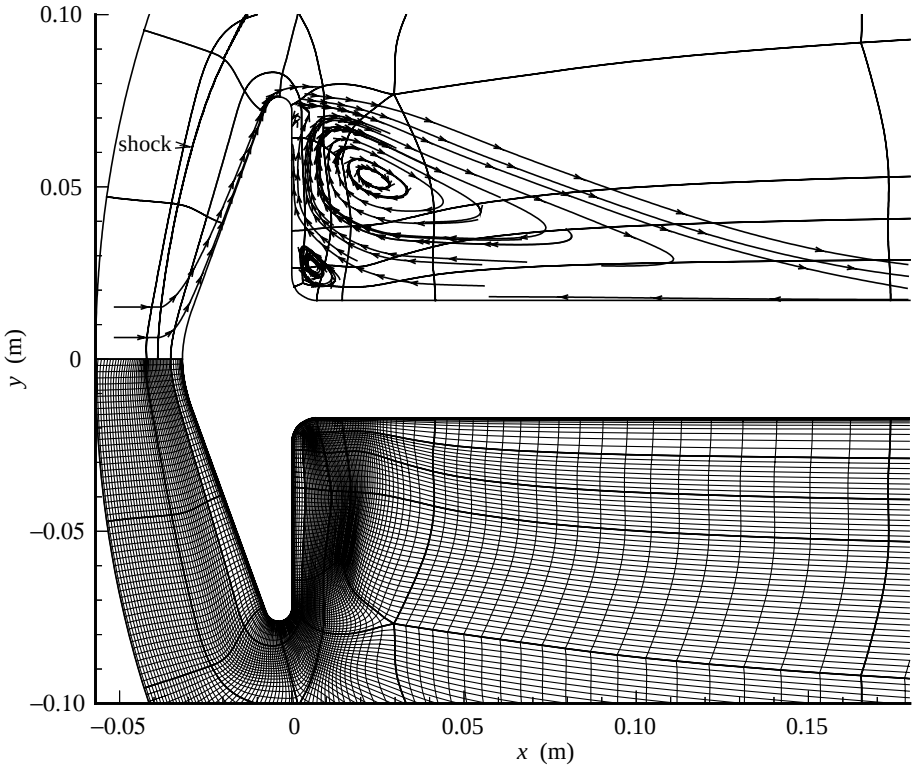

Figure 27. Streamline pattern and bow shock (F4: condition III), and multiblock mesh topology (43 blocks; coarse).

validation purposes, but also as a standard model for facility-to-facility comparison (Saric *et al.* 1996). The geometry is given in figure 24. The objective was to test the same model in different high-enthalpy facilities, all having the same reservoir conditions; to study non-equilibrium expansion processes around the blunt-cone shoulder; to investigate the separation point, shear-layer dynamics and wake closure; and to study reattachment heating on the sting. The common reservoir point in terms of enthalpy and pressure was 10 MJ kg^{-1} and 500 bar. In the past, experiments have been carried out in the LENS facility, in the HEG and extensively in the Langley perfect-gas Mach 6 and 10 facilities. Recent publications by Horvath *et al.* (1996, 1997) and Holden *et al.* (1997) summarized very well the numerical as well as the experimental work done on the blunt cone. Figures 25 and 26 provide a summary of the principal hypersonic experiments done on the blunt cone for the forebody and the afterbody sting, respectively. These suggest that the only laminar experiment was the LENS run 22 (centreline) and that all the others exhibited transition in the shear layer. Here we will report on the recent blunt-cone experiments performed in the ONERA F4 facility for the so-called match point (500 bar, 10 MJ kg^{-1}), i.e. for the F4 condition III, and for two other reservoir conditions (II and IV); and we report on attempts to analyse numerically the shear layer reattachment heating on the sting using non-equilibrium Navier–Stokes codes, TINA and LORE, as well as the DSMC code SMILE (Muylaert *et al.* 1997).

The forebody was instrumented with 40 Chromel–constantan coaxial thermocou-

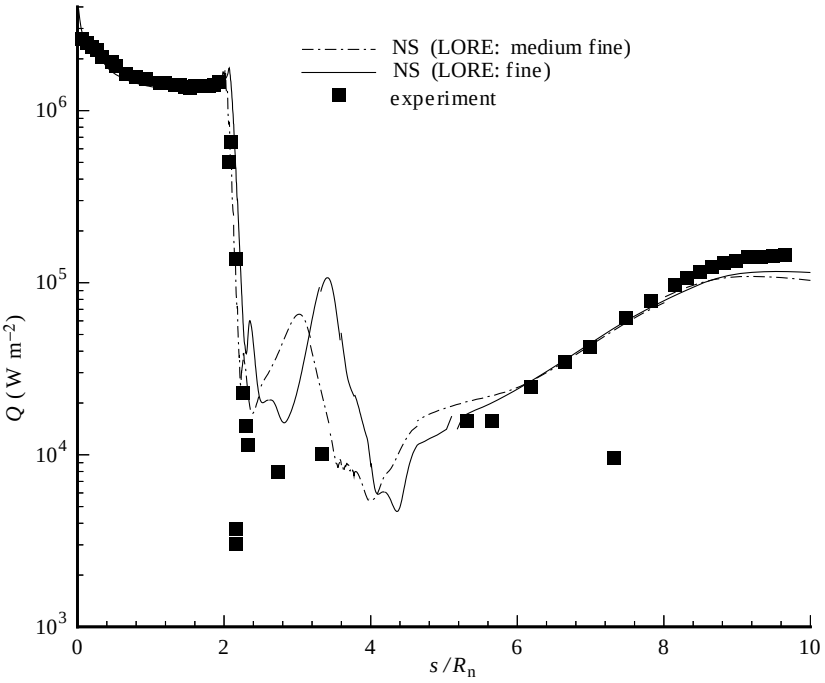

Figure 28. Comparison of NS with experimental data (F4: condition III).

ples along a ray, whereas the base and the sting were instrumented with 65 thin-film resistance gauges. Coaxial thermocouples were selected for use on the forebody because of their small size, fast response and durability from particle damage during testing in the HEG and the LENS facilities, as explained in Horvath *et al.* (1996). The F4 test conditions are shown in table 3.

(*a*) *Forebody and afterbody analysis*

The numerical tools used for the analysis are the Navier–Stokes codes TINA and LORE and the DSMC code SMILE as explained by Muylaert *et al.* (1997).

Fully catalytic wall boundary conditions were used. Figure 27 shows the topology of the coarse grid combined with the wake streamline patterns of interest. For the F4 (condition III), grid refinements were carried out using a coarse mesh with 200×75 points, a normal mesh with 400×150 points and a fine mesh with 800×300 points. For the finest grid, normal resolution of the first grid point is 10^{-7} m.

The comparisons with the experiments for two of the three F4 conditions as from table 3 are shown in figures 28 and 29. The forebody heating results are in excellent agreement. The interest lies in the wake and therefore the data are plotted on a log scale to enhance differences in the wake region. Figure 28 also shows results for the two finest grids. It will be shown below that the reattachment region in the experiment for condition III is non-laminar. The good experimental/numerical comparison for condition IV confirms that the flow is fully laminar.

Before starting turbulent computation the full Navier–Stokes equations were used and compared with the thin-layer approximation. To our surprise the predicted heating at reattachment gave better agreement with experiment and additional peak-

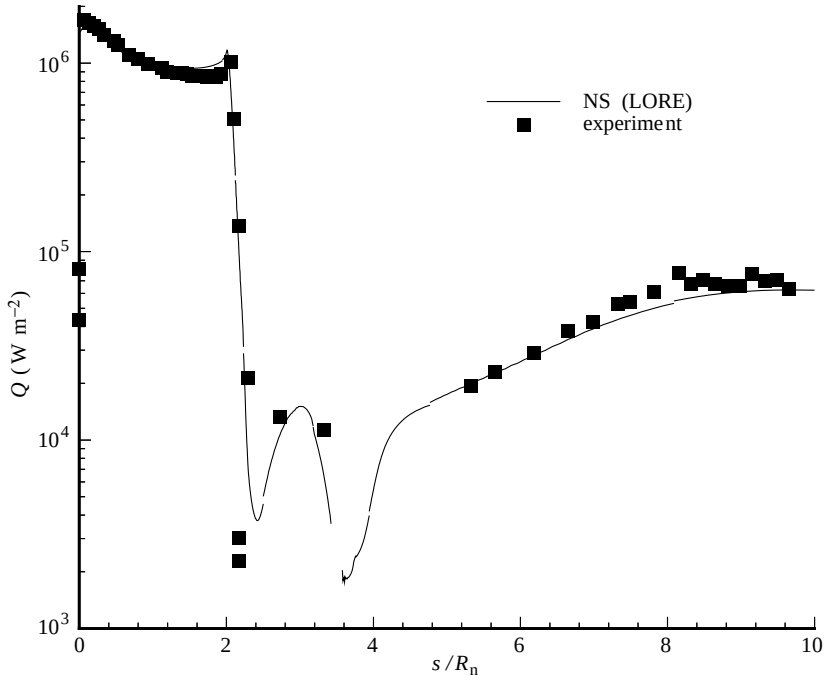

Figure 29. Comparison of NS with experimental data (F4: condition IV).

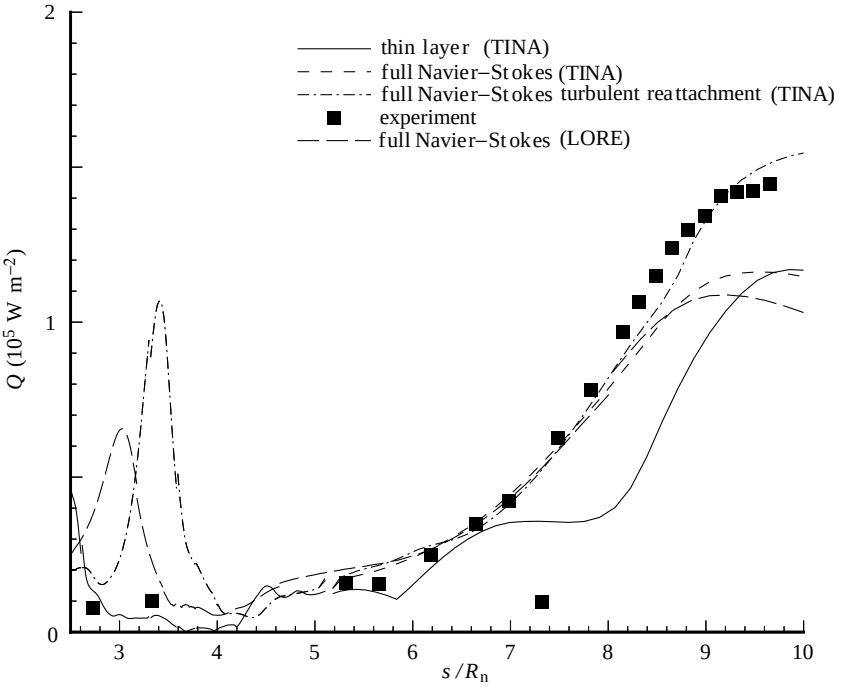

Figure 30. Reattachment heating laminar/turbulent.

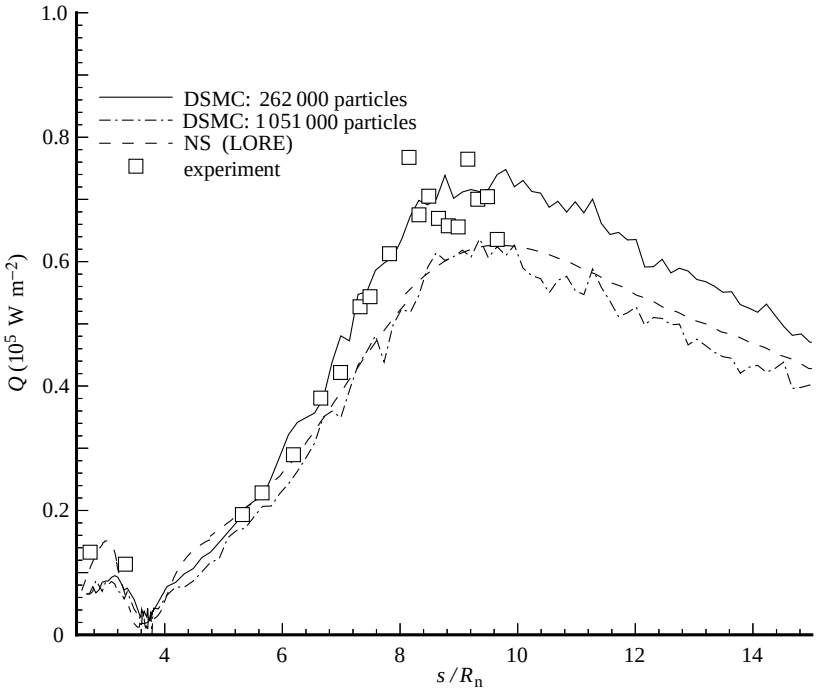

Figure 31. Comparison of DSMC with experimental data and NS (F4: condition IV).

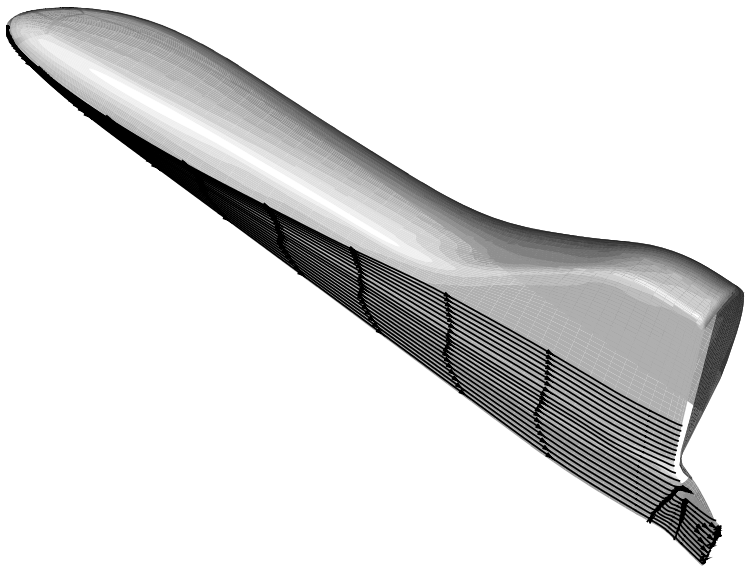

Figure 32. Halis configuration.

Table 4. *Free-stream conditions Halis*

	flight	F4	S4	HEG
reduced enthalpy	330	160	14	278
total pressure (bar)		280	25	450
M_∞	24.3	8.4	9.8	9.6
altitude (km)	72.4			
T_∞ (K)	213	795		
$\rho L/U10^{-5}$	0.28	0.044	3.6	0.12
$Re_{\mathrm{ref}\cdot L}10^6$	10.3	.28	20.1	0.54

heating levels appeared associated with secondary vortex reattachment in the base region (see figure 30). The difference in shear flow and subsequent wake-flow characteristics due to the omission of the higher-order viscous terms in the full Navier–Stokes equations used for the thin-layer approximation is something that requires further research. In order to study transition at reattachment, the boundary layer in one block on the sting was switched to turbulent conditions using the Baldwin–Lomax model. In this one block the boundary layer upstream and downstream of separation is still attached and so as a first approximation Baldwin–Lomax could be used. The match with the experiments is very good.

Figure 31 shows the comparison with the DSMC SMILE code. The results are very good for condition IV where the remaining discrepancy is less than 10%.

8. Halis

The objective here is to investigate the extent to which the use of high-enthalpy facilities can contribute to the validation of ground-to-flight extrapolation and more specifically to the validation of real-gas effects (Perier *et al.* 1996). The test case chosen is the US Orbiter, for which some flight data exist in the open literature. Figure 32 shows the Halis configuration, which is the generic configuration duplicating the windward side of the orbiter. It is well known that during its first re-entry the US Orbiter experienced a so-called 'pitch-up anomaly' due to real-gas effects on both the spacecraft pitching moment and control surface effectiveness (C_m with body-flap deflected minus C_m with body-flap undeflected). A discrepancy in pitching moment coefficient of 0.03 for the Orbiter, corresponding to a body-flap deflection of *ca.* 8°, was experienced.

The pitching moment is defined (with a reference area of 250 m^2 (Orbiter wing area) and a reference length of 12.6 m) to act about the centre of gravity, which is taken to be at $0.65L$, with L the Orbiter length being 32.77 m. We will show pitching moments as measured in the S4 perfect-gas facility, compared with results from F4 and compared with flight. The European reference perfect-gas facility is the S4 Mach 10 blow-down facility, which has good flow quality and accurate measurement techniques. The reservoir pressure was selected to avoid transition effects. The F4 and HEG facilities represent two intermediate steps between S4 and flight in the process of extrapolation to flight conditions.

The baseline flight point is: STS2 time, 75 620 s; Mach number, 24.3; altitude, 72.3 km; angle of attack, 39.4°; elevon deflection, 1.7°; body-flap deflection, 14.9°.

Table 5. *Calculated pitching moment coefficients around the centre of gravity*

	flight comp. ESTEC	F4 comp. ESTEC	F4 exp. ONERA	
BF 0	−0.017	−0.0429	−0.022	zero body-flap deflection
BF 15	−0.0683	−0.076	−0.060	15° body-flap deflection

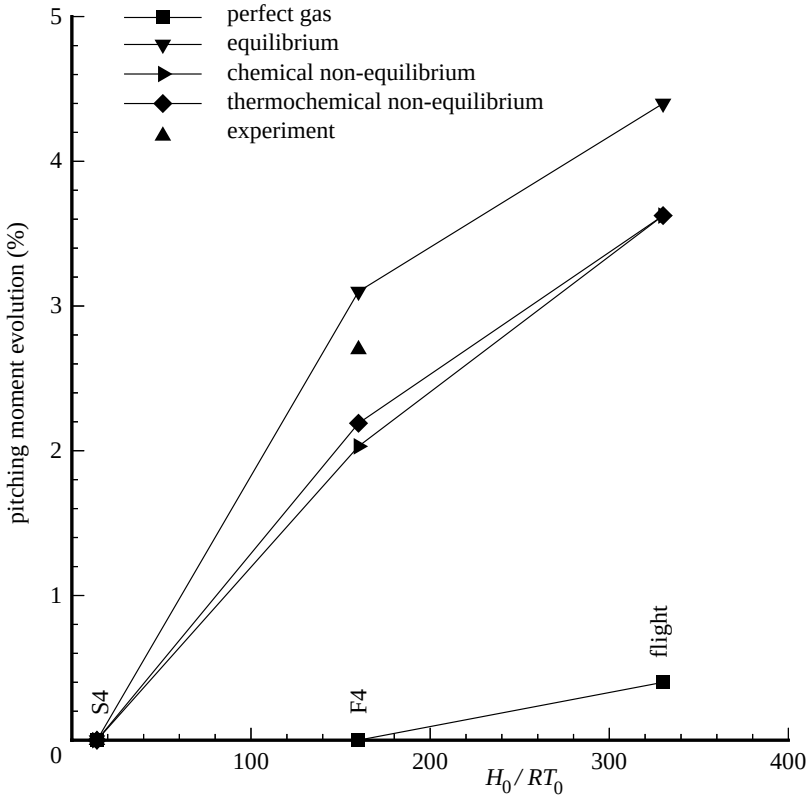

Figure 33. Orbiter pitching-moment evolution versus reduced enthalpy in S4, F4 and flight (zero body-flap deflection).

Computations were performed by Dassault, EPFL and ONERA (Perier *et al.* 1996) with Euler and boundary-layer codes including approximations for viscous interaction. The conditions are summarized in table 4.

Force measurements were performed in S4 and F4 on an Orbiter model at 40° angle of attack both with 0 and 15° body-flap deflection. Figures 33 and 34 summarize these results in terms of pitching moment coefficient versus enthalpy. The S4 pitching moments were subtracted to serve as reference. It is clear from those charts that a pitch-up of the order of 0.03 has been measured between S4 and F4 conditions. More precisely, it can be seen that this pitch-up is more important on the clean configuration than on that with the body flap deflected, which means that the effectiveness is increased (by *ca.* 20%). The pressure coefficient distribution along

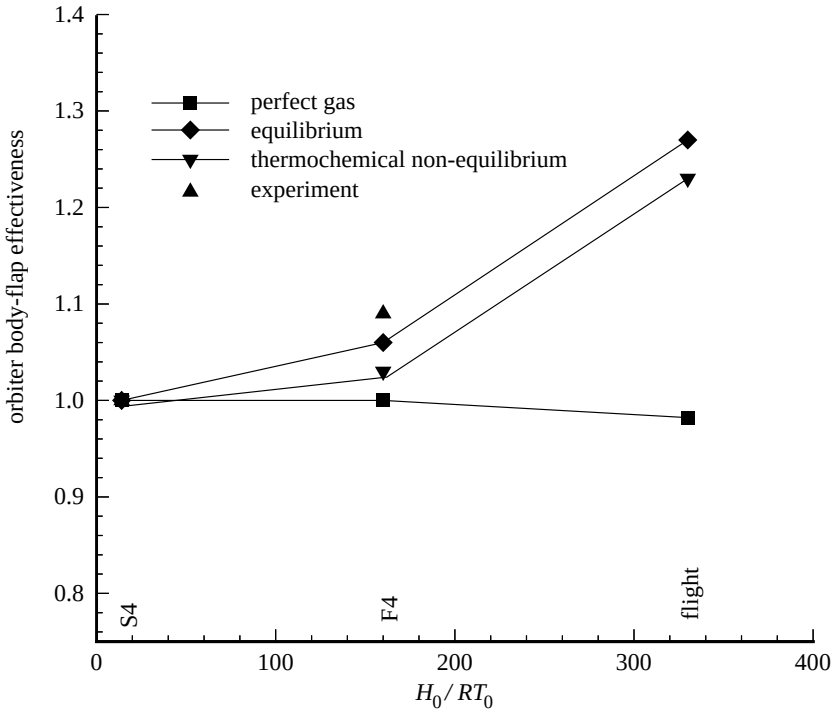

Figure 34. Orbiter body-flap effectiveness versus reduced enthalpy in S4, F4 and flight.

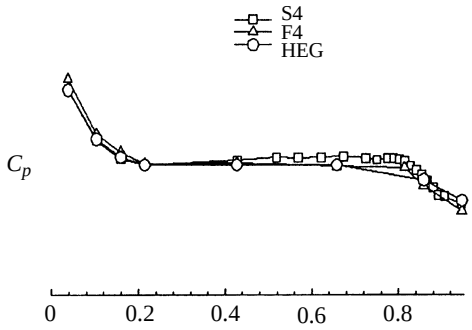

Figure 35. Halis centreline pressure coefficient distributions for S4, F4 and HEG for flight and F4 conditions.

the windward centreline is presented in figure 35 for S4, F4 and the HEG for the non-deflected body flap. These distributions confirm the pitch-up described earlier between S4 and F4 data since one can notice a small pressure increase at the nose and a larger decrease at the rear.

Table 5 compares the wind-tunnel and flight-computed pitching moment coefficients with those measured in F4 (Spel *et al*. 1997).

Figure 36 compares the centreline pressure coefficients measured in F4 with those computed with TINA with and without body-flap deflection. An increase in flap-pressure coefficient (combined with a reduction in separated flow in front of the body flap) is seen when extrapolating from F4 to flight conditions.

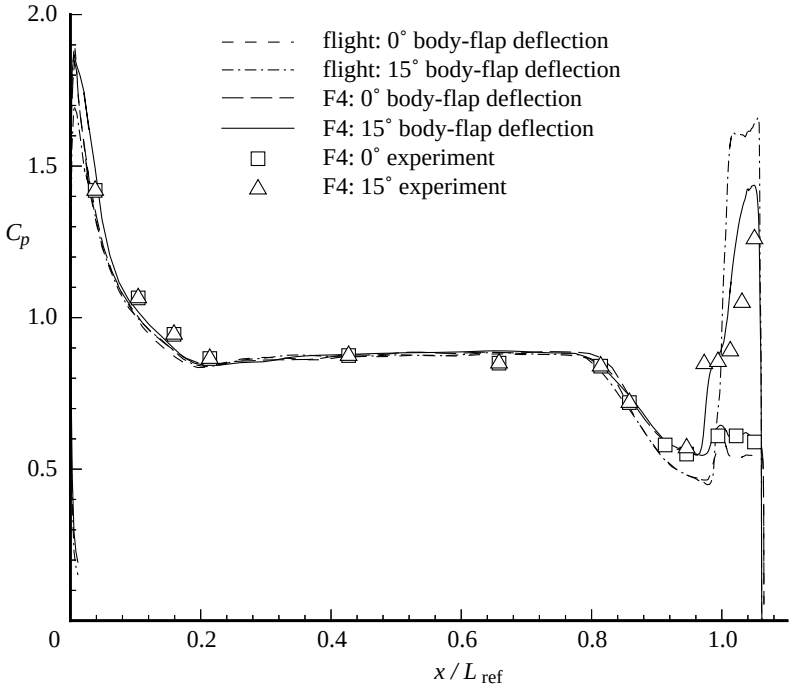

Figure 36. Halis windward pressure coefficient distribution in F4. (C_p measured along centreline at $\alpha = 40°$.)

9. Future perspectives

In the future it is clear that computational fluid dynamics (CFD) will play a more dominant role; but not at the expense of experimental testing. The role of the wind tunnels will change: the R & D facilities will be used more for the validation of physical modelling, whereas the industrial wind tunnels will be used for static and dynamic database generation.

The use of CFD will be progressively and continuously increased

(1) in the design of experiments, the definition of the test environment, the development, application and interpretation of diagnostics and in the analysis of the results; the test data will then form a basis for validating this process including CFD tools; and

(2) for the extrapolation from wind tunnel to flight conditions. The flight data will then be used to qualify the whole process.

10. Concluding remarks

The status of facilities for hypersonic testing in Europe has been enhanced significantly in the past ten years; results from these facilities are already used to validate codes and provide vehicle design information. Future missions can be foreseen that will force the technical community to improve our competence in suitably instrumented facilities, CFD and flight testing. The role of CFD in the design process will undoubtedly be increased, but not at the expense of testing.

Nomenclature

ARD	atmospheric re-entry demonstrator
AS CP	C_p computation done by Aerospatiale
C_{m}	pitching moment coefficient
C_p	pressure coefficient
CELHYO	an ONERA Navier–Stokes tool
CIRA	Centro Italiano Ricerche Aerospaziale
DLR	Deutsche Forschungsanstalt fur Luft- und Raumfahrt
DSMC	direct simulation Monte Carlo
EPFL	Ecole Polytechnique Federale de Lausanne
ESTEC	European Space Research and Technology Centre
F.D.S.	flux difference splitting
F.V.S.	flux vector splitting
H_0	reservoir enthalpy
HOMAR	an ONERA Navier–Stokes tool
ITAM	Institute of Theoretical and Applied Mechanics
LaRC	NASA Langley Research Center
LADS	laser diode spectroscopy
LENS	large energy national shock tube
LORE	an ESTEC Navier–Stokes tool
NO	nitric oxide
NS	Navier–Stokes
ONERA	Office National d'Études et de Recherches Aerospatiales
PANASCE	an ONERA Navier–Stokes tool
PNS	parabolized Navier–Stokes
Q	heat flux
R	gas constant
R_{Electre}	nose radius of the Electre model
RCP	reference control point
s	distance along the wall
SMILE	the ITAM DSMC tool
T_{v}	vibrational temperature
TINA	an ESTEC Navier–Stokes tool, from Fluid Gravity Engineering (FGE) Ltd, Liphook, UK
VDR	vibration–dissociation–recombination
VUB	Vrije Universiteit Brussels

The authors thank Dr Hannemann from DLR and Dr Sagnier from ONERA for their most valuable contributions throughout this review paper.

References

Durand, G., Schwane, R. & Muylaert, J. 1997 ESA Manned Space Transportation programme. In *Proc. of the Aerothermodynamics Workshop*, YPA/2254/JM.

Holden, M., Harvey, J., Boyd, I., George, J. & Horvath, T. 1997 Experimental and computational studies of the flow over a sting mounted planetary probe configuration. In *AIAA 32nd Aerospace Sciences, Meeting & Exhibit, Reno, NV*, AIAA paper 97-0768.

Horvath, T., McGinley, C. & Hannemann, K. 1996 Blunt body near wake flow field at Mach 6. In *27th Fluid Dynamics Conf., New Orleans, LA*, AIAA paper 96-1935.

Horvath, T., McGinley, C. & Hannemann, K. 1997 Blunt body near wake flow field at Mach 10. In *27th Fluid Dynamics Conf., Reno, NV*, AIAA paper 97-0986.

Muylaert, J., Walpot, L., Steijl, R. & Spel, M. 1997 Blunt cone near wake analysis in F4 and Lens. In *21st Int. Symp. on Shock Waves (ISSW), Queensland, Australia*, paper 6555.

Muylaert, J., Walpot, L., Spel, M., Sagnier, P., Hannemann, K. & Olivier, H. 1998 A review of European code validation in high enthalpy flow. In *AIAA 20th Advanced Measurement and Ground Testing Conference, Albuquerque, NM*, AIAA paper 6555.

Perier, P., Rapuc, M., Rostand, P., Sagnier, P., Verant, J., Eitelberg, G., Bogstad, M. & Muylaert, J. 1996 Ground to flight extrapolation of reentry aircraft aerodynamics: an experimental and computational approach. In *AIAA 14th Applied Aerodynamics Conf., New Orleans, LA*, AIAA paper 96-2434.

Sagnier, P. & Verant, J. 1998 Flow characteristics in the ONERA high enthalpy wind tunnel.

Saric, B., Muylaert, J. & Dujarric, C. 1996 Hypersonic experimental and computational capability, improvement and validation. AGARD-AR-319, vol. 1.

Schwane, R. 1996 Description of test cases. MSTP 1996 workshop on re-entry aerothermodynamics and ground-to-flight extrapolation. Technical report document YPA/1356/RS, ESA-ESTEC.

Simeonides, G., Walpot, L., Netterfield, M., Tumino, G. & Muylaert, J. 1996 Evaluation of engineering heat transfer prediction methods in high enthalpy flow conditions. In *AIAA 31th Thermophysics Conf., New Orleans, LA*, AIAA paper 96-1860.

Spel, M., Steijl, R., Muylaert, J. & Haeuser, J. 1997 Testing and numerical rebuilding of Halis in high enthalpy conditions. In *21st Int. Symp. on Shock Waves (ISSW), Queensland, Australia*, paper 6554.

Walpot, L. & Bakker, P. 1997 Development and validation of a three-dimensional thermochemical non-equilibrium Navier–Stokes solver. Technical Report Memorandum-815, T.U. Delft.

Walpot, L. & Kordulla, W. 1996 Synthesis of the Electre in the hypersonic impulse facility HEG. In *Proc. of the Aerodynamics Workshop, ESTEC, Noordwijk, The Netherlands.*